Quaternary Science Reviews 290 (2022) 107644

Contents lists available at ScienceDirect

Quaternary Science Reviews

journal homepage: www.elsevier.com/locate/quascirev

Invited review

The influence of lateral Earth structure on inferences of global ice volume during the Last Glacial Maximum

Linda Pan [a,*], Glenn A. Milne [b], Konstantin Latychev [a], Samuel L. Goldberg [c], Jacqueline Austermann [d], Mark J. Hoggard [e], Jerry X. Mitrovica [a]

[a] Department of Earth and Planetary Sciences, Harvard University, USA
[b] Department of Earth and Environmental Sciences, University of Ottawa, Canada
[c] Department of Earth, Atmospheric and Planetary Sciences, Massachusetts Institute of Technology, USA
[d] Lamont-Doherty Earth Observatory, Columbia University, USA
[e] Research School of Earth Sciences, Australian National University, Australia

A R T I C L E I N F O

Article history:
Received 28 March 2022
Received in revised form
30 June 2022
Accepted 4 July 2022
Available online xxx

Handling Editor: C. O'Cofaigh

Keywords:
Last glacial maximum
Sea-level change
Glacial isostatic adjustment
Global ice volume
Numerical modeling

A B S T R A C T

The mapping between far-field relative sea level (RSL) records and changes in ice volume or global mean sea level (GMSL) involves a correction for glacial isostatic adjustment (GIA). This mapping is thus sensitive to uncertainties inherent to GIA modeling, including the spatio-temporal history of ice mass changes and viscoelastic Earth structure. Here, we investigate the effect of incorporating lateral variations in Earth structure on predicting far-field sea level in order to determine if this source of model uncertainty significantly impacts estimates of global ice volume at the Last Glacial Maximum (LGM). We consider a set of forty 3-D simulations that sample different Earth model parameters: the adopted lithospheric thickness, the seismic velocity model used to infer lateral temperature variations, the scaling factor used in the conversion from temperature to viscosity, and the spherically averaged "background" viscosity profile. In addition, we consider results based on two ice histories. We present global maps of the differences between these simulations and a set of 1-D simulations at the LGM, as well as RSL histories at 5 locations that have been previously considered in estimates of ice volume at LGM: Barbados, two sites at the Great Barrier Reef, Bonaparte Gulf and Sunda Shelf. We find that the difference between inferences of global mean sea level (GMSL) at LGM based on 3-D and 1-D Earth models peaks in Barbados with differences ranging from ~2.5 to 11 m, with a mean of ~6–7 m. At the other sites, the difference ranges from ~2 to −8 m, with mean differences between ~0 and −3 m. After comparing different pairs of simulations, we conclude that, in general, the impact of varying the seismic model, lithospheric thickness model, background 1-D model, and scaling factor from temperature to viscosity is significant at far-field sites. Finally, while we do not find a consistent signal at the above far-field sites that would help to reconcile the LGM ice volumes estimated from GIA studies and those estimated from summing regional ice sheet reconstructions, the impact is nonetheless large enough that GIA analyses of RSL records in the far field of ice sheets should include 3-D viscoelastic Earth models.

1. Introduction

Reconstructions of global ice volume at the Last Glacial Maximum (LGM; Clark et al., 2009) are widely explored in studies of glacial isostatic adjustment (GIA) and ice age climate. Various methodologies have been adopted in such studies. One method of inferring ice volume is based on oxygen isotope variability within sedimentary cores (e.g., Waelbroeck et al., 2002). However, this approach is complicated by the confounding effects associated with temperature, local salinity and the location of the ice mass flux (Raymo et al., 2018). A second method is based on GIA modeling, whereby the ice budget is inferred from fits to regional sea-level datasets and local constraints on ice geometry (e.g., Lambeck et al., 2017; Lambeck et al., 1998) or by tuning the total ice budget to match sea-level curves from the far field of the Pleistocene ice sheets (e.g., Nakada et al., 2016; Peltier and Fairbanks,

* Corresponding author. Department of Earth and Planetary Sciences, 20 Oxford St., Cambridge, MA, 02138, USA.
E-mail address: lindapan@g.harvard.edu (L. Pan).

https://doi.org/10.1016/j.quascirev.2022.107644

2006). Finally, ice sheet modeling, whether combined with GIA modeling (e.g., Gomez et al., 2020; Tarasov et al., 2012) or not (e.g., Abe-Ouchi et al., 2013; Whitehouse et al., 2012) have also provided constraints on LGM ice volume. Here, we revisit the method that uses far-field relative sea-level (RSL) data with the aim to quantify a potential bias in the estimated ice volume associated with the common GIA model assumption of a spherically-symmetric Earth viscosity structure.

In the 1970s and 1980s, the Climate Long-range Investigation, Mapping and Prediction (CLIMAP) project provided the first global reconstruction of climate during the LGM, including a minimum and a maximum reconstruction of ice sheet volumes (Denton and Hughes, 1981). The minimum ice reconstruction located ice margins near continental margins and was characterized by a global ice volume of ~127 m, in units of equivalent global mean sea level (GMSL). The maximum ice reconstruction, in contrast, featured expanded marine-based ice sheets and a global ice volume of ~163 m GMSL equivalent. Although subsequent field evidence (Dyke et al., 2002; Miller et al., 2002) and GIA modeling (e.g., Yokoyama et al., 2000) have suggested ice cover that was less extensive than the maximum ice reconstruction, it has nevertheless been commonly used as a boundary condition in climate and general circulation models (Clark and Mix, 2002). (Note that global sea-level change has other contributions beyond changes in ice mass, including changes in salinity and temperature. The term barystatic sea level has recently been adopted to distinguish the contribution of ice mass flux to GMSL change from other contributions (Gregory et al., 2019); however, we will continue to use GMSL throughout this paper since it is widely adopted within the paleoclimate literature.)

Following CLIMAP, the Environmental Processes of the Ice-Age: Land, Oceans, Glaciers (EPILOG) program began in 1999 with the aim of developing a comprehensive reconstruction of Earth during the LGM, using updated data and methods as well as accounting for advances made since CLIMAP (Mix et al., 2001). This program inferred minimum and maximum ice volumes of ~118 m and 130–135 m GMSL equivalent. The EPILOG reconstructions were characterized by ice sheet margins that were largely consistent with the CLIMAP maximum ice reconstruction but with a significantly different distribution of ice thickness (Clark and Mix, 2002).

In terms of GIA-based estimates of ice volumes, Peltier and colleagues have iteratively revised a global ice model history, publishing the ICE-6G model in 2015 (Peltier et al., 2015) and more recently, the ICE-7G model (Roy and Peltier, 2017). Differences between the two are relatively minor, with an identical ice-loading history for all regions outside of North America. Our study adopts the more widely used ICE-6G model. The detailed space-time variation in the ICE-6G model is constrained using a variety of near field data, including ice margin chronologies, RSL records, and GPS measurements of crustal motion and gravity observations associated with the Gravity Recovery and Climate Experiment (GRACE). The total excess ice volume (volume of ice in excess of present-day ice volume) at LGM was tuned to fit the coral-inferred RSL record at Barbados. In this regard, LGM in the model occurs at ~26 ka with an excess ice volume of ~127 m GMSL equivalent, where ~14 m of that total resides in Antarctica. This GIA-based inference is coupled to the assumed viscoelastic Earth structure, and, in particular, the one-dimensional VM5a viscosity profile, which represents a multilayer fit to the VM2 viscosity model used in developing the earlier ICE-5G ice history (Peltier, 2004). The VM5a model involves a moderate increase in viscosity with depth, increasing from 5×10^{20} Pa s in the upper mantle to 3×10^{21} Pa s in the deep mantle.

Lambeck et al. (2014) used an extensive set of ~1000 RSL sediment and coral records from various locations in the far field of ice sheets to constrain the time history of integrated ice volume from 35 ka to present day using GIA modeling. Their preferred "high viscosity" Earth model yielded peak excess ice mass during LGM (21 ka) of ~134 m equivalent GMSL, with an Antarctic component of ~23 m, inferred from the difference between total ice volume and the sum of Northern Hemisphere ice volumes and mountain glaciers. Their "low viscosity" solution suggested an excess ice mass at LGM ~7 m equivalent GMSL more than the preferred "high viscosity" solution, with an excess Antarctic ice mass of ~30 m. Following Lambeck et al. (2014), Yokoyama et al. (2018) used well-dated fossil corals and coralline algae assemblages collected from the Great Barrier Reef to infer GMSL changes. Their study found an LGM low stand of 125–130 m equivalent GMSL that occurred at ~20.5 ka. As in Peltier et al. (2015), both studies adopted 1-D viscosity profiles in their GIA modeling.

The above GIA-based estimates suggest global ice volumes during the LGM in the range of ~125–135 m equivalent GMSL with an excess Antarctic ice mass component of 14–30 m. While the majority of the latter range cannot be excluded when limitations associated with data and model uncertainty as well as the completeness of the observational record are considered (Briggs et al., 2014; Lecavalier and Tarasov, 2021), a growing number of ice sheet and climate modeling studies constrain this value to be less than ~10 m (e.g., Golledge et al., 2013; Ivins et al., 2013; Whitehouse et al., 2012). Gomez et al. (2013) also favor these lower estimates based on results from coupled ice sheet-sea level modeling experiments. If GIA studies of far-field RSL histories require a total excess ice volume of 125–135 m, and the Antarctic component likely does not exceed ~10 m, the question arises as to where these studies can increase ice mass flux outside Antarctica to compensate for the latter bound. This issue, which is also evident in post-LGM ice volume reconstructions (e.g., Cuzzone et al., 2016), has come to be known as the "missing ice" problem (Austermann et al., 2013; Clark and Tarasov, 2014; Simms et al., 2019). A recent ice sheet reconstruction developed using near-field ice extent and sea-level data (Gowan et al., 2021) contains an LGM ice volume of 116 m equivalent GMSL and is reported to match observed LGM RSL lowstands.

While the detailed methodologies used to estimate global ice volume at LGM based on far-field RSL records differ, they all involve a correction or estimate of the geographically variable signal of the GIA process. As a consequence, these studies are sensitive to model uncertainties of two types (Briggs and Tarasov, 2013; Melini and Spada, 2019): (1) those associated with limited knowledge of model inputs, such as the spatio-temporal history of ice mass changes and viscoelastic Earth structure (so-called "parametric uncertainty"); and (2) those associated with inaccuracy of the forward model related to, for example, missing or poorly represented physical processes or simplifications in model set up (so-called "structural uncertainty"). A growing number of studies have sought to quantify GIA model uncertainty associated with one or both of these aspects using different approaches (e.g., Caron et al., 2018; Love et al., 2016; Simon and Riva, 2020).

Common simplifications of GIA models that could lead to significant structural error in some regions include: (1) the assumption of a Maxwell rheology and thus neglect of non-linear deformation and transient signals in the Earth response (e.g., Ivins et al., 2022; Kang et al., 2022; Lau et al., 2021; Ranalli, 2001; van der Wal et al., 2013; Wu and Wang, 2008), and (2) the application of spherically-symmetric Earth models and thus neglect of lateral variations in Earth structure, including elastic lithospheric thickness and mantle viscosity (e.g., Li et al., 2018; Paulson et al., 2007; van der Wal et al., 2013). Most efforts to examine and quantify this second simplification as a source of structural uncertainty have focused on near-field regions (e.g., Li et al., 2020; van der Wal et al., 2013). Austermann et al. (2013) presented the first attempt to explore this issue at a far-field location. Their study demonstrated that lateral variations in mantle viscosity in the vicinity of Barbados, in particular the presence of a high viscosity slab associated with the subduction of the Caribbean Plate, would suppress post-LGM crustal subsidence (and thus sea-level rise) associated with ocean loading in the region. They concluded that the total excess ice volume at LGM must be increased by ~7 m equivalent GMSL relative to inferences based on standard 1-D Earth modeling to maintain a fit to the coral record of RSL change at Barbados — a requirement that accentuates the "missing ice" problem. More generally, their results highlight that failing to include lateral variations in Earth structure can lead to a significant bias in estimates of LGM ice volume based on GIA modeling.

In the present study, we extend the analysis of Austermann et al. (2013) to consider a much wider range of 3-D GIA simulations and assess the impact of this added model complexity and realism across the entire far field of ancient ice cover. In addition to global maps of this impact, we also present results at far-field sites that have been a particular focus of previous GIA modeling of the LGM sea level low stand, including the Great Barrier Reef, Bonaparte Gulf, Sunda Shelf, and Barbados.

2. Methods

We present model output from a total of 40 simulations that include different realizations of 3-D Earth structure, along with predictions based on three 1-D Earth viscosity models for comparison. These simulations allow us to explore the influence of specific parameter choices on quantifying lateral variations in Earth viscosity structure and to assess the sensitivity of our GIA predictions to ice history and specific features of the 3-D Earth models, including lithospheric thickness, the globally averaged "background" 1-D viscosity model, and the magnitude and spatial variation (from different seismic models) of lateral variations in mantle viscosity. A summary of the primary model inputs varied in this study is provided in Table 1.

We use two global ice histories to generate simulations of RSL: ICE-6G (Peltier et al., 2015) and a model we label as ANU (Lambeck et al., 2014). The 1-D Earth models used in this study are those that are typically associated with these ice histories. In the case of ICE-6G, we adopt a version of the VM2 viscosity profile (Peltier, 2004). This version has a 3-layer viscosity profile, where the upper mantle viscosity is 4×10^{20} Pa s, the top ~1100 km of the lower mantle has a viscosity of 2.2×10^{21} Pa s, and the remainder of the lower mantle has a viscosity of 3.3×10^{21} Pa s. ICE-6G is generally paired with the VM5 viscosity model (Peltier et al., 2015), but the 3-layer approximation of VM2 used here is very similar in both viscosity amplitudes and depth parametrization. Thus, the impact of this choice of viscosity model on our study is minor. Two classes of Earth models are favored in the adoption of the ANU ice history. In the first, the increase in viscosity from upper to lower mantle is greater than two orders of magnitude and in the second, this increase is approximately one order of magnitude (Lambeck et al., 2014). We sample both classes using a lithospheric thickness of 71 km, and upper and lower mantle pairings for both the preferred model of Lambeck et al. (2014), (2×10^{20} Pa s, 3×10^{22} Pa s), and their second solution, (3×10^{20} Pa s, 2×10^{21} Pa s). We label these models $M1D_A$ and $M1D_B$, respectively. We note that, while our chosen values do not correspond to the optimal values found in Lambeck et al. (2014), they do lie within the identified 1-σ uncertainty ranges. For example, we chose a lower mantle viscosity of 3×10^{22} Pas rather than 7×10^{22} Pas for $M1D_A$ based on the growing number of studies that suggest the smaller value is more accurate when additional datasets are considered (e.g., Hill et al., 2019; Lau et al., 2016; Nakada et al., 2015). The 3-D Earth viscosity models that we consider in this study adopt, in a spherically averaged sense, one of the three 1-D models described above.

Lithospheric thickness variations are adopted from two published models: Afonso et al. (2019) and Yousefi et al. (2021). The former is based on the inversion of geophysical and geochemical data to infer various properties of the lithosphere and upper mantle, including temperature. In this model, the lithospheric thickness is defined thermally by specifying the base of the lithosphere as coinciding with a given isotherm within the upper mantle model. We label this model AF. In the second model (Yousefi et al., 2021), which we label YO, lithospheric (elastic) thickness in continental regions is taken from previously published models of lithospheric (elastic) thickness based on the spatial coherence of gravity and elevation data (Audet and Burgmann, 2011; Chen et al., 2017; Steffen et al., 2018). In ocean areas, it is defined thermally using sea-floor age to determine the local geotherm and assigning a given isotherm to define the base of the lithosphere. Further details on these two models can be found in the cited publications. In our analysis, these models are scaled to give the global mean of the adopted 'background' 1-D model (i.e., 71 km when using ANU ice history, or 96 km when using ICE-6G). Fig. 1 shows both models in the case where they have been scaled so that their global average matches the lithospheric thickness of the 1-D ANU model (71 km). In AF and YO, the minimum lithospheric thickness is ~15 km and ~25 km (when scaled such that the global average is 71 km), respectively, and tends to occur near mid-ocean ridges. Maximum thicknesses, reaching ~200−350 km, are typically found in cold cratonic areas of continents. Such large values are partly a result of

Table 1
Summary of the primary model inputs varied in this study.

Parameter	Model/Range	Reference
Lithospheric thickness	AF	Afonso et al. (2019)
	YO	Yousefi et al. (2021)
Seismic velocity	S40RTS	Ritsema et al. (2011)
	Savani	Auer et al. (2014)
	SEMUCB-WM1	French and Romanowicz (2014)
	SL2013sv	Schaeffer and Lebedev (2013)
Background viscosity (Pa s)	$M1D_A$ (Upper mantle: 2×10^{20} ; Lower mantle: 3×10^{22})	Lambeck et al. (2014)
	$M1D_B$ (Upper mantle: 3×10^{20} ; Lower mantle: 2×10^{21})	Lambeck et al. (2014)
	VM2 (Upper mantle: 4×10^{20} ; Top ~1100 km of lower mantle: 2.2×10^{21} ; Remainder of lower mantle: 3.3×10^{21})	Peltier (2004)
Temperature to viscosity scaling (ϵ; $^{o}C^{-1}$)	0.02 or 0.04	Austermann et al. (2013)

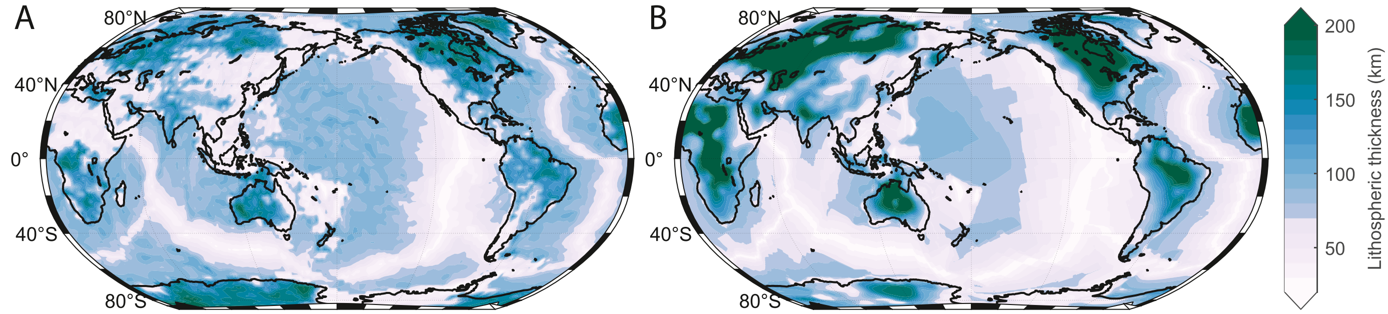

Fig. 1. Lithospheric thickness models used in this study, scaled to have an average thickness of 71 km. (A) AF by Afonso et al. (2019) and (B) YO by Yousefi et al. (2021).

scaling the laterally variable lithosphere models to give a global average thickness that is equivalent to a given 1-D reference viscosity model. Some areas have large spatial gradients but are mainly found in continental regions, such as western to central North America. The AF model tends to have more smaller scale structure when compared to the YO model.

We determined four models of lateral variation in mantle viscosity using published global seismic tomographic models (Auer et al., 2014; French and Romanowicz, 2014; Ritsema et al., 2011; Schaeffer and Lebedev, 2013). Milne et al. (2018) described and compared these four global seismic velocity models. These models of lateral variations in viscosity are superimposed on the three 1-D models described earlier. Our mapping from seismic wave speed anomalies to viscosity can be described by the following three equations (Latychev et al., 2005):

$$\delta ln\rho(\mathrm{r},\theta,\varphi) = \frac{\partial ln\rho}{\partial \mathrm{ln}v_s}(\mathrm{r})\delta lnv_s(\mathrm{r},\theta,\varphi) \tag{1}$$

$$\delta T(\mathrm{r},\theta,\varphi) = -\frac{1}{\alpha(\mathrm{r})}\delta ln\rho(\mathrm{r},\theta,\varphi) \tag{2}$$

$$\eta(\mathrm{r},\theta,\varphi) = \eta_0(\mathrm{r})\mathrm{e}^{-\varepsilon\delta\mathrm{T}(\mathrm{r},\theta,\varphi)} \tag{3}$$

where $r, \theta,$ and φ are the radius, colatitude, and east-longitude, and $v_s, \rho, T,$ and η are seismic wave speed, density, temperature, and viscosity. The parameter α is the depth-dependent coefficient of thermal expansion, and $\frac{\partial ln\rho}{\partial \mathrm{ln}v_s}$ is a depth-dependent scaling between seismic velocity anomaly and density. The conversion from seismic wave speed to temperature and viscosity involves a number of assumptions and the use of parameters that are poorly known. A detailed discussion of this topic can be found in Ivins et al. (2021; Section 2.4). The parameters used here are the same as those adopted in Austermann et al. (2013). The parameter ε in equation (3) governs the strength of the exponential dependence of viscosity on temperature, and thus the peak-to-peak lateral variability of the former for a given input velocity model. In this study, we consider two scaling factors: 0.04 and 0.02 $^{\circ}\mathrm{C}^{-1}$. Decreasing the scaling factor from 0.04 to 0.02 $^{\circ}\mathrm{C}^{-1}$ decreases the order of magnitude of the calculated range in lateral viscosity variation by approximately a factor of two over some depth extent in the mantle.

Viscosity variations at two depths, 346 km and 1071 km, based on the S40RTS (Ritsema et al., 2011) and Savani (Auer et al., 2014) seismic tomography models and a scaling factor of 0.04 $^{\circ}\mathrm{C}^{-1}$ are shown in Fig. 2. At 346 km, S40RTS and Savani both have viscosity variations that span several orders of magnitude. For most grid cells (99%), the variation at this depth is within about 4 orders of magnitude for each seismic model shown in Fig. 2 (range of roughly ± 2 orders magnitude about the 1-D reference value). The viscosity variation at 1071 km is larger than that at 346 km, with 99% of the values for S40RTS spanning about 7 orders of magnitude (-2.9 to 3.9 about the 1-D reference value) and those for Savani spanning about 6.5 orders of magnitude (-3 to 3.4). These ranges are relatively large compared to estimates based on mineral physics considerations (e.g., Karato, 2008) and so we consider them to represent an upper bound (for the adopted seismic model). The regions of high viscosity in both models tend to be associated with areas of active subduction, such as the Malay Archipelago. There are also significant differences between the two models. For instance, there are some regions where the two models have opposite signs in viscosity variations, such as the province of Québec, eastern Canada at 346 km depth and the West Indian Ocean at 1071 km depth.

We calculate gravitationally self-consistent sea-level change for each ice history and Earth model pairing (ICE-6G with VM2 and the VM2-based 3-D Earth models; ANU with the two corresponding 1-D Earth models and the 3-D models based upon them). We adopt the algorithm of Kendall et al. (2005) for solving the generalized sea-level equation of Mitrovica and Milne (2003). The calculations assume a Maxwell viscoelastic Earth model and accurately account for time-varying shorelines and rotational effects on sea level. The latter is computed using the rotational stability theory of Mitrovica et al. (2005) which accounts for the observed oblateness of the Earth. All computations are performed using the finite volume software described in detail by Latychev et al. (2005). The computational domain is defined by a total of ~17 million nodes with 67 radial layers and a spatial resolution of ~60 km at the base of the mantle to ~12 km at the Earth's surface. Given the large model domain and the three iterations that are required to accurately compute paleotopography (and thus shoreline position), a single model run is computationally expensive. To provide a rough measure of this expense, one simulation beginning at 36 ka takes several days using ~100 compute cores.

With an aim to reduce model run time, we ran some tests to determine how sensitive predictions of LGM RSL are to the timing of model initiation. A major increase in global ice volume prior to the LGM occurs after ~36 ka in each of the chosen ice models. Therefore, this age represents a possible minimum (latest) initiation time that would accurately capture LGM sea level, and this is the initiation time used in all simulations presented in this study. To test the accuracy of neglecting pre-36 ka loading changes, we performed two additional simulations (one 3-D and one 1-D) which began at 80 ka. Predictions of the impact of lateral viscosity variations on RSL at LGM for simulations that differ only on the start time (Fig. S1) indicate that adopting the shorter duration

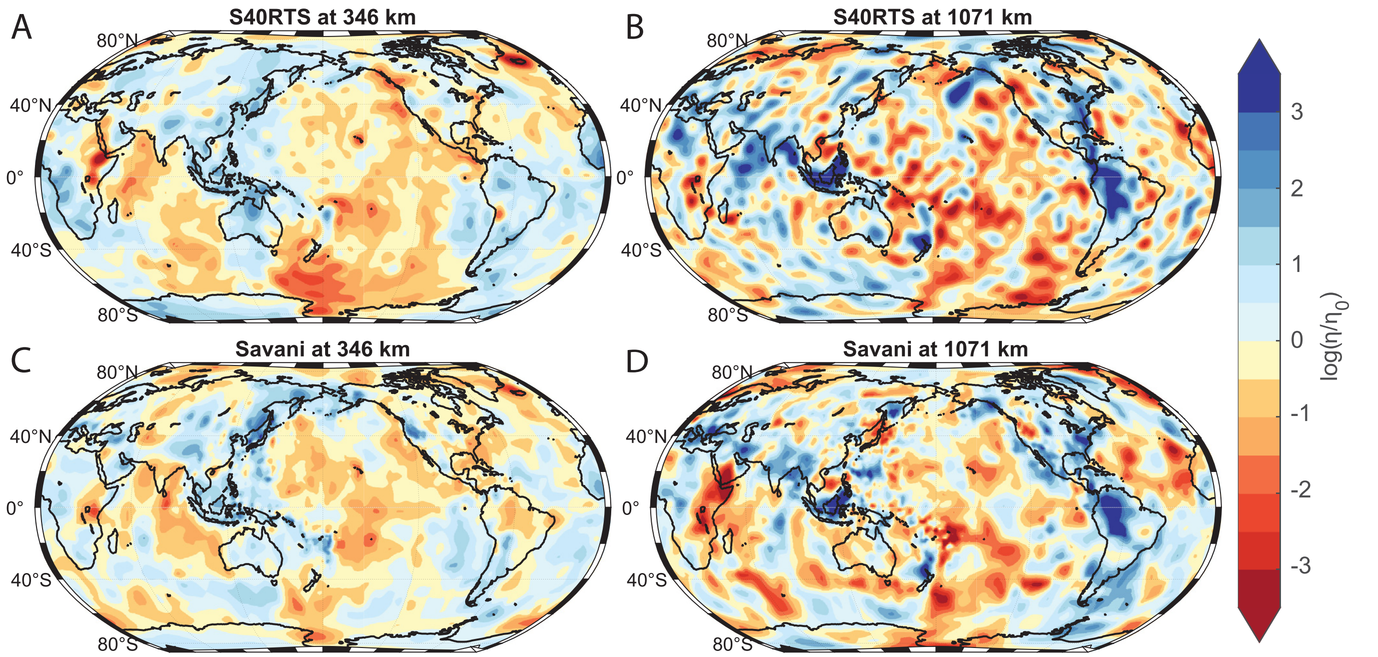

Fig. 2. Lateral viscosity variations relative to the spherically averaged background value based on the S40RTS (A and B; Ritsema et al., 2011) and Savani (C and D; Auer et al., 2014) seismic models at 346 km depth (A and C), and 1071 km depth (B and D). The results shown are based on an ε value of 0.04 °C^{-1} (eq. (3)).

introduces small, order 0.1 m, errors at far-field sites.

Accounting for both ice histories, the three associated background 1-D Earth models, the two models of variations in lithospheric thickness, the four seismic models, and the two temperature-to-viscosity scaling factors, there is a total of 40 simulations (24 using the ANU ice history, and 16 using ICE-6G) that include lateral variations in Earth structure (Table 2). Note that for the $M1D_B$ viscosity model adopted with the ANU ice model, only one ε value was considered (0.04 °C^{-1}). We also consider three simulations in which we do not include lateral variations in Earth structure (one for each of the background 1-D models associated with the two ice histories) to isolate the importance of lateral structure on LGM ice volume by considering the difference between the 3-D and 1-D simulations.

Table 2
Specifications of each of the 40 simulations.

Name of Simulation	Ice history	Lithospheric thickness	Viscosity structure	Reference 1-D Model	Scaling factor (°C^{-1})
AF_$M1D_A$S40	ANU	AF	S40RTS	$M1D_A$	0.04
AF_$M1D_A$SAV	ANU	AF	Savani	$M1D_A$	0.04
AF_$M1D_A$SEM	ANU	AF	SEMUCB-WM1	$M1D_A$	0.04
AF_$M1D_A$SL	ANU	AF	SL2013sv	$M1D_A$	0.04
AF_$M1D_B$S40	ANU	AF	S40RTS	$M1D_B$	0.04
AF_$M1D_B$SAV	ANU	AF	Savani	$M1D_B$	0.04
AF_$M1D_B$SEM	ANU	AF	SEMUCB-WM1	$M1D_B$	0.04
AF_$M1D_B$SL	ANU	AF	SL2013sv	$M1D_B$	0.04
YO_$M1D_A$S40	ANU	YO	S40RTS	$M1D_A$	0.04
YO_$M1D_A$SAV	ANU	YO	Savani	$M1D_A$	0.04
YO_$M1D_A$SEM	ANU	YO	SEMUCB-WM1	$M1D_A$	0.04
YO_$M1D_A$SL	ANU	YO	SL2013sv	$M1D_A$	0.04
YO_$M1D_B$S40	ANU	YO	S40RTS	$M1D_B$	0.04
YO_$M1D_B$SAV	ANU	YO	Savani	$M1D_B$	0.04
YO_$M1D_B$SEM	ANU	YO	SEMUCB-WM1	$M1D_B$	0.04
YO_$M1D_B$SL	ANU	YO	SL2013sv	$M1D_B$	0.04
ep02AF_$M1D_A$S40	ANU	AF	S40RTS	$M1D_A$	0.02
ep02AF_$M1D_A$SAV	ANU	AF	Savani	$M1D_A$	0.02
ep02AF_$M1D_A$SEM	ANU	AF	SEMUCB-WM1	$M1D_A$	0.02
ep02AF_$M1D_A$SL	ANU	AF	SL2013sv	$M1D_A$	0.02
ep02YO_$M1D_A$S40	ANU	YO	S40RTS	$M1D_A$	0.02
ep02YO_$M1D_A$SAV	ANU	YO	Savani	$M1D_A$	0.02
ep02YO_$M1D_A$SEM	ANU	YO	SEMUCB-WM1	$M1D_A$	0.02
ep02YO_$M1D_A$SL	ANU	YO	SL2013sv	$M1D_A$	0.02
AF_96VM2_S40	ICE-6G	AF	S40RTS	96VM2	0.04

(continued on next page)

Table 2 (*continued*)

Name of Simulation	Ice history	Lithospheric thickness	Viscosity structure	Reference 1-D Model	Scaling factor ($^{\circ}C^{-1}$)
AF_96VM2_SAV	ICE-6G	AF	Savani	96VM2	0.04
AF_96VM2_SEM	ICE-6G	AF	SEMUCB-WM1	96VM2	0.04
AF_96VM2_SL	ICE-6G	AF	SL2013sv	96VM2	0.04
YO_96VM2_S40	ICE-6G	YO	S40RTS	96VM2	0.04
YO_96VM2_SAV	ICE-6G	YO	Savani	96VM2	0.04
YO_96VM2_SEM	ICE-6G	YO	SEMUCB-WM1	96VM2	0.04
YO_96VM2_SL	ICE-6G	YO	SL2013sv	96VM2	0.04
ep02AF_96VM2_S40	ICE-6G	AF	S40RTS	96VM2	0.02
ep02AF_96VM2_SAV	ICE-6G	AF	Savani	96VM2	0.02
ep02AF_96VM2_SEM	ICE-6G	AF	SEMUCB-WM1	96VM2	0.02
ep02AF_96VM2_SL	ICE-6G	AF	SL2013sv	96VM2	0.02
ep02YO_96VM2_S40	ICE-6G	YO	S40RTS	96VM2	0.02
ep02YO_96VM2_SAV	ICE-6G	YO	Savani	96VM2	0.02
ep02YO_96VM2_SEM	ICE-6G	YO	SEMUCB-WM1	96VM2	0.02
ep02YO_96VM2_SL	ICE-6G	YO	SL2013sv	96VM2	0.02

3. Results and discussion

3.1. Spatial patterns and amplitudes

We computed the difference between predictions of RSL at LGM (26 ka for the ICE-6G ice history and 21 ka for the ANU ice history, i.e., when global ice volume is maximum for each ice model) based on each of the 3-D simulations in Table 2 and those based on the associated background 1-D model. Global maps of the mean and standard deviation of these runs, partitioned between the two ice histories, are shown in Fig. 3. The results for these two loading cases are qualitatively similar at low latitudes indicating that the impact of lateral variations in viscosity on predictions of far-field RSL at LGM is relatively insensitive to details of the ice history. At locations where the mean 3D-1D model output is positive (blue in Fig. 3A and B), such as Barbados, the sea-level prediction based on a 3-D Earth model is shallower (RSL is less negative) than the 1-D case, and therefore has a smaller post-LGM sea-level change. Thus, if LGM ice volume was to be inferred from one of these locations, the use of model calculations made with a 1-D Earth model would result in an underestimate (since less global ice melt is required to match the observed RSL rise). In contrast, at locations where the mean 3D-1D model difference is negative, such as Noggin Pass, ice volume inferences made from the 1-D GIA calculation would lead to an overestimate. Finally, the mean effect of lateral Earth structure is relatively small at locations near the white band, such as Hawai'i.

The similarity between the two sets of results with distinct ice histories is reinforced in Fig. 4A, where we show the peak magnitude of Fig. 3A and B as a function of latitude (solid lines) as well as the standard deviation computed at the site at which the peak magnitude occurs (dashed lines). The location of each site is shown in Fig. 4B. These magnitudes increase rapidly as one considers latitudes that sample the peripheral bulge of the Laurentide Ice Sheet (above ~20°N) and the West Antarctic Ice Sheet (below

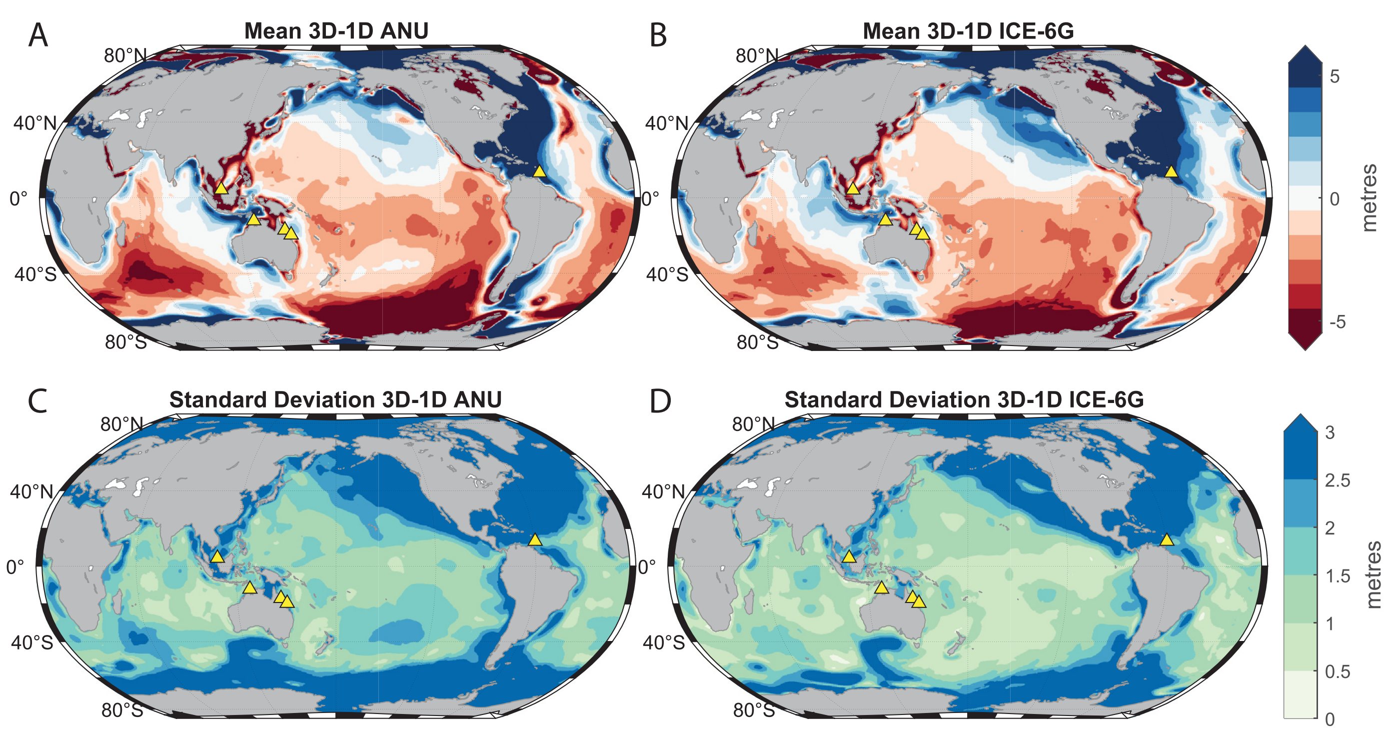

Fig. 3. Mean (A, B) and standard deviation (C, D) of the difference between predictions of RSL at LGM computed with the 3-D Earth model and the associated 1-D spherical average (background) Earth model. (A, C) include simulations based on the ANU ice history, and (B, D) are simulations using ICE-6G. Yellow triangles show the locations of sites in Fig. 5.

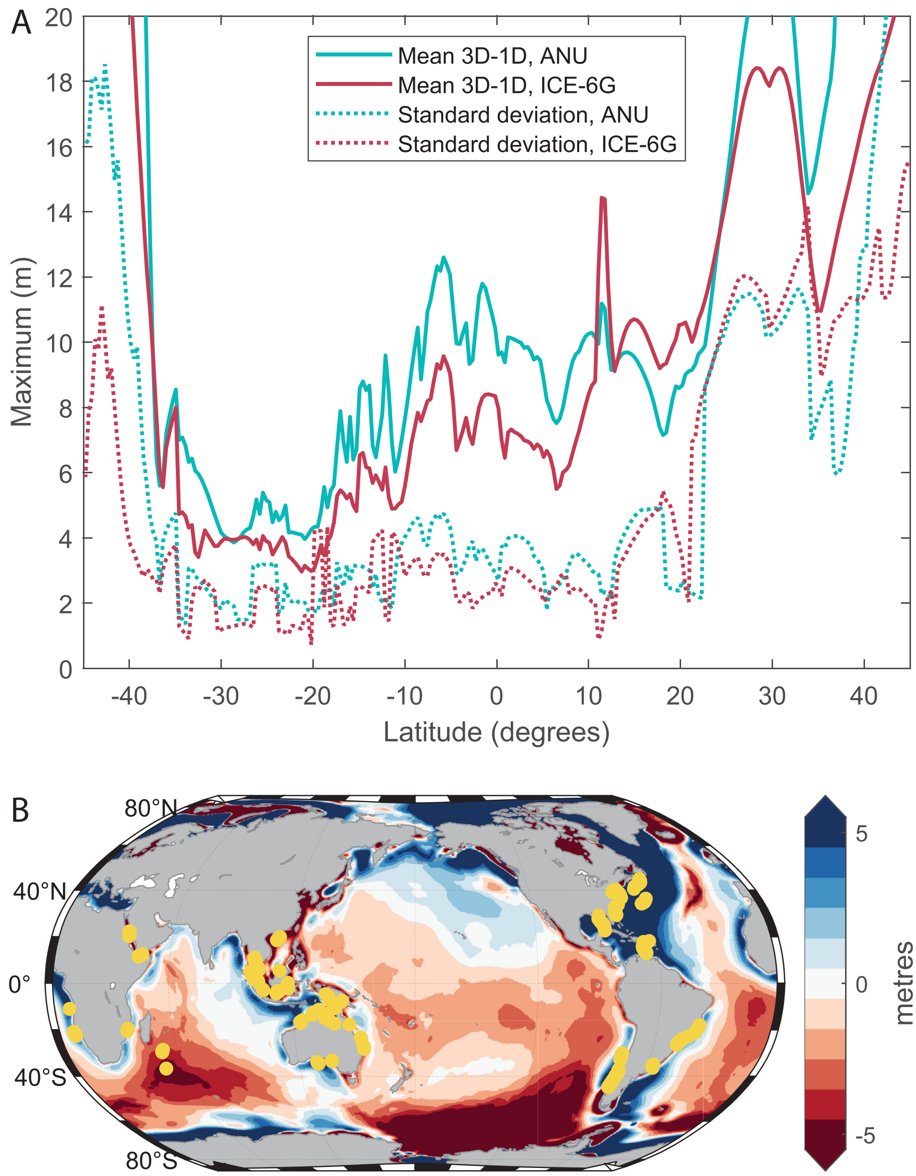

Fig. 4. (A) Maximum magnitude of the mean RSL difference shown in Fig. 3A and B as a function of latitude (45°S to 45°N) based on the ANU (solid turquoise line) and ICE-6G (solid red line) ice histories. For every latitude in the degree 512 Gauss-Legendre grid, we find the maximum difference and the longitude at which it occurs. The dashed lines of associated color show the standard deviation of the simulations at the site of maximum magnitude. (B) Same as Fig. 3A but with yellow dots plotted at every latitude in the grid from 45°S to 45°N to show the location of the site of maximum magnitude at that latitude.

~35°S), reaching a few 10s of m. In the former region, these large amplitudes are likely due to the larger lithospheric thickness values and higher than average viscosity in the shallow upper mantle over North America and the western North Atlantic Ocean. These two characteristics would suppress the signal of the peripheral bulge in the western North Atlantic Ocean, leading to a smaller post-LGM RSL rise. The southern Pacific Ocean has a thin oceanic lithosphere and viscosities in West Antarctica are lower than average, leading to enhanced deformation and a larger post-LGM rise for the 3-D case in this region.

Between ~20°N and ~35°S, the peak magnitude of the mean difference between the 3-D and 1-D results varies between ~4 m and ~12 m, with a trend toward higher values moving northward. At very low latitudes, i.e., between ±20°N, the sites showing the largest difference between the 3-D and 1-D simulations tend to be clustered in Southeast Asia and the Caribbean, close to local subduction zones, as well as the northern margin of Australia and in the Red Sea. There is also a large difference in the Indian ocean, which is likely associated with the Central Indian Ocean Triple Junction. The lithosphere around the triple junction is thin, leading to a larger ocean-loading signal and thus a larger post-LGM RSL rise. Finally, the standard deviation ranges from ~1 to 4 m at the locations of peak mean difference; it is highly correlated with the signal amplitude and is significant, reaching ~30–50% of the signal.

3.2. *Far-field sites*

We next consider the LGM RSL predictions for the individual simulations (relative to the associated 1-D case) at 5 far-field sites with published RSL data from the LGM: Barbados, Sunda Shelf, Bonaparte Gulf, Noggin Pass, and Hydrographer's Passage (Table 3). One way to estimate the effect of the inclusion of lateral variations

Table 3
The difference between predictions of RSL at LGM computed with the 3-D Earth model and the associated 1-D spherically averaged (background) Earth model. The mean, median, and standard deviation of each group of simulations (grouped by background Earth model) are also included.

Name of Run	Barbados	Sunda Shelf	Bonaparte Gulf	Noggin Pass	Hydrographer's Passage
AF_M1D$_A$S40	6.12	-2.39	-0.83	-1.84	-1.28
AF_M1D$_A$SAV	6.59	-1.60	-0.39	-2.74	-2.07
AF_M1D$_A$SEM	7.00	-4.07	-1.13	-3.96	-2.99
AF_M1D$_A$SL	5.88	0.03	-0.68	-2.77	-1.67
YO_M1D$_A$S40	6.89	-1.25	-0.36	-0.90	-0.16
YO_M1D$_A$SAV	6.36	-0.68	0.18	-1.93	-0.84
YO_M1D$_A$SEM	7.08	-3.54	-0.73	-3.03	-2.14
YO_M1D$_A$SL	5.99	0.36	-0.16	-1.88	-0.69
ep02AF_M1D$_A$S40	2.57	-1.55	0.94	-1.77	-0.89
ep02AF_M1D$_A$SAV	2.82	-0.72	0.38	-2.14	-1.20
ep02AF_M1D$_A$SEM	3.34	-2.40	0.43	-2.78	-1.42
ep02AF_M1D$_A$SL	2.83	1.44	0.26	-1.73	-0.37
ep02YO_M1D$_A$S40	4.21	-0.90	2.09	-0.51	0.72
ep02YO_M1D$_A$SAV	3.76	-0.32	1.59	-1.09	0.37
ep02YO_M1D$_A$SEM	4.40	-2.04	1.58	-1.62	-0.08
ep02YO_M1D$_A$SL	3.79	1.80	1.56	-0.50	1.05
MEAN	4.98	-1.11	0.29	-1.95	-0.85
MEDIAN	5.14	-1.08	0.22	-1.86	-0.86
STANDARD DEVIATION	1.66	1.61	1.00	0.95	1.09
AF_M1DBS40	8.41	-4.27	-2.35	-5.05	-2.80
AF_M1DBSAV	10.97	-3.78	-2.36	-5.60	-3.37
AF_M1DBSEM	9.55	-6.72	-3.54	-8.23	-5.30
AF_M1DBSL	7.38	0.27	-0.46	-3.47	-0.57
YO_M1DBS40	8.27	-3.41	-2.05	-4.40	-2.51
YO_M1DBSAV	10.36	-3.05	-1.77	-4.92	-2.83
YO_M1DBSEM	9.34	-6.33	-3.33	-7.42	-5.16
YO_M1DBSL	7.26	0.48	-0.37	-3.04	-0.79
MEAN	8.94	-3.35	-2.03	-5.27	-2.92
MEDIAN	8.88	-3.60	-2.20	-4.98	-2.82
STANDARD DEVIATION	1.34	2.65	1.16	1.80	1.74
AF_96VM2_S40	9.65	-2.78	-0.40	-3.11	-1.97
AF_96VM2_SAV	10.52	-2.13	-0.57	-3.46	-2.42
AF_96VM2_SEM	9.20	-5.10	-1.42	-5.65	-4.20
AF_96VM2_SL	6.31	1.02	0.25	-2.30	-1.12
YO_96VM2_S40	9.83	-2.49	-0.25	-2.54	-1.19
YO_96VM2_SAV	10.25	-2.16	0.11	-2.84	-1.46
YO_96VM2_SEM	8.88	-5.48	-1.16	-4.80	-3.32
YO_96VM2_SL	6.38	0.68	0.60	-1.75	-0.09
ep02AF_96VM2_S40	4.53	-1.73	0.98	-1.83	-1.39
ep02AF_96VM2_SAV	5.74	-1.38	0.38	-1.95	-1.55
ep02AF_96VM2_SEM	5.24	-3.88	0.39	-3.22	-2.23
ep02AF_96VM2_SL	3.59	0.73	0.45	-1.66	-1.01
ep02YO_96VM2_S40	4.94	-1.62	1.76	-1.03	-0.12
ep02YO_96VM2_SAV	5.95	-1.54	1.48	-1.23	-0.21
ep02YO_96VM2_SEM	5.27	-3.93	1.14	-2.23	-0.98
ep02YO_96VM2_SL	4.02	0.56	1.43	-0.89	0.47
MEAN	6.89	-1.95	0.32	-2.53	-1.42
MEDIAN	6.13	-1.93	0.39	-2.27	-1.29
STANDARD DEVIATION	2.41	2.02	0.92	1.31	1.22
TOTAL MEAN	6.54	-1.90	-0.16	-2.85	-1.49
TOTAL MEDIAN	6.33	-1.67	-0.02	-2.42	-1.24
TOTAL STD DEV	2.42	2.12	1.36	1.78	1.47

in Earth structure on inferences of LGM ice volume from RSL data is to look at the average effect over all simulations and all 5 sites. The mean difference between 3-D and 1-D simulations is ~0.03 m, with a standard deviation of ~3.9 m. The median gives a similar result of approximately −0.9 m, and thus the average effect of lateral structure on LGM sea-level predictions is close to 0. However, as the effect of including lateral Earth structure on sea-level predictions is geographically variable (Figs. 3 and 4), it is informative to consider model results at individual sites. Even at a single site, there can be a large degree of variability across simulations. For example, the difference between 3-D and 1-D simulations spans ~8.5 m at Sunda Shelf and ~7.5 m at Noggin Pass. This large variability reflects the uncertainty in defining the 3-D viscosity structure. At Noggin Pass, for instance, one of the 3-D simulations (ep02YO_M1D$_A$SL, Table 2) suggests that the incorporation of lateral viscosity structure would change the estimate of LGM ice volume by ~0.5 m when compared to the reference 1-D simulation. A different simulation (AF_M1D$_B$_SEM, Table 2) suggests that the LGM ice volume estimate could be over 8 m less than the 1-D inference. Furthermore, if one were to consider a single 3-D simulation at Barbados, the conclusion could be that estimates of LGM ice volume should be increased by nearly 11 m (e.g., AF_M1D$_B$SAV, Table 2). This highlights the importance of considering data from multiple sites as well as estimating the uncertainty related to assigning 3-D viscosity structure.

We can also consider Table 3 in conjunction with Fig. 5, which shows the time series of sea-level change computed with the ANU ice history at the same 5 far-field sites. The magnitude of the difference between 3-D and 1-D simulations at the LGM using the ANU ice model varies from site to site and ranges from ~0 to nearly 11 m (Fig. 5; Table 3). Analogous results based on the ICE-6G ice history are shown in Fig. S2. The range of variability in the 3-D simulations is comparable to the range in the 1-D simulations, at least at the 5 sites considered here. The site where the impact of lateral variations in mantle viscosity is largest is Barbados, with a mean difference (3-D minus 1-D) of 5.0 m, 8.9 m and 6.9 m, and a standard deviation of 1.7 m, 1.3 m, and 2.3 m for 3-D simulations adopting the 1-D background models of M1D$_A$, M1D$_B$ and VM2, respectively. The average difference in LGM RSL between 3-D and 1-D predictions of all the simulations at Barbados is 6.5 m with a total standard deviation of 2.4 m, so the signal is large and the associated uncertainty is comparatively small. The magnitude and sign of these values are consistent with the 3-D GIA simulations of Austermann et al. (2013), who found that lateral stucture perturbed the 1-D prediction by ~7 m. Note that in all simulations, the 3-D prediction of RSL at LGM at Barbados is shallower (i.e., there is a smaller post-LGM sea-level rise) than the associated 1-D prediction, indicating that the interpretation described by Austermann et al. (2013) – an ocean-loading induced reduction of crustal subsidence due to the high viscosity slab beneath the site and/or a change in the dynamics of the peripheral bulge – are universal features of the 3-D model runs presented here.

At the Noggin Pass site, offshore of Australia and on the Great Barrier Reef, introducing lateral variations in Earth viscosity structure also perturbs predictions of RSL at LGM in a consistent manner, with an average signal amplitude that exceeds the standard deviation. However, in contrast to Barbados, the effect is to deepen the LGM low stand by 0.5–8.2 m (with a mean of ~ −2.9 and an associated standard deviation of 1.8 m), which, if used to infer LGM ice volume, would lead to a lower estimate than that based on a 1-D model. At this site, the 3-D Earth models are characterized by a significantly thinner lithosphere (~38 km in AF and ~56 km in YO) than the associated 1-D model used as a background state (Fig. 1) and thus ocean loading post-LGM would drive a larger offshore crustal subsidence (and sea-level rise) associated with so-called “continental levering” (Clark et al., 1978; Nakada and Lambeck, 1989). A similar interpretation could apply for Hydrographer's Passage on the Great Barrier Reef, although a small number of 3-D simulations do predict a shallowing of the low stand relative to the 1-D case.

At Sunda Shelf, the mean difference between 3-D and 1-D simulations is −1.9 m, with a standard deviation of similar magnitude (2.1 m). While the estimated model uncertainty is of a similar size as the signal, most of the simulations show a deepening of the LGM low stand, suggesting that lateral Earth structure is contributing to a consistent offset. Lambeck et al. (2002) have shown that there is a large ocean loading signal at Sunda Shelf, which is likely affected by lateral variations in Earth structure. Fig. 1 shows that the lithosphere is thinner than average (71 km), ~40–45 km in both 3-D models of lithospheric thickness at this location, which may lead to an amplification of the ocean loading signal. We also note that the largest signals at Sunda Shelf tend to occur with the model we labeled SEM (French and Romanowicz, 2014). Fig. S3 shows viscosity variations in the SEM model at 346 km and 1071 km depth. Beneath the Sunda Shelf, the SEM model is ~1 order of magnitude less viscous than S40RTS and just under 1 order of magnitude less viscous than Savani at 346 km depth, which likely also contributes to the amplification of the ocean loading signal. Finally, at Bonaparte Gulf, the impact of lateral variations in mantle structure on RSL at LGM can be of either sign, and the mean value of the perturbation is relatively small.

3.3. Isolating parameter sensitivities

To explore the sensitivity of the results to individual aspects of the adopted 3-D Earth model, we begin with a map (Fig. 6A) showing the difference between a prediction of RSL at LGM for the run adopting the Ritsema et al. (2011) seismic tomography model S40RTS, the lithospheric thickness variations given by Afonso et al. (2019), a temperature-to-viscosity scaling factor of 0.04 $^{\circ}C^{-1}$, a spherical average background structure M1D$_A$, and the 1-D simulation based on M1D$_A$. Within 20° of the equator, the magnitude peaks at ~10 m in the area close to Barbados and the northern shoreline of South America and ~16 m in Makassar Strait just east of Borneo. As we noted above, the largest signals are evident close to subduction zones, where high viscosity subducted slabs impact solid Earth deformation, and on continental margins, where the continental levering signal can be strongly affected by variations in lithospheric thickness (and asthenospheric viscosity).

Next, we alter one aspect in the construction of the 3-D model, including the adopted seismic tomography model, lithospheric thickness model, background 1-D model, and scaling factor from temperature to viscosity (Fig. 6B–E, respectively). Comparison of the model results in Fig. 6B–E with 6A suggests that adopting a different lithospheric thickness model has the smallest impact on predicted far-field RSL differences in most regions, albeit in simulations in which the global averages of the two lithospheric thickness models are the same. There are significant differences near some mid-ocean ridges, where the YO lithosphere model tends to give lower RSL values than AF. A change in the temperature to viscosity scaling factor (ε) also has a relatively small effect in most regions, which may reflect the relatively long wavelength of the S40RTS seismic tomography model (Ritsema et al., 2011). There is also a spatial correlation between Fig. 6A and E, showing that the main effect of reducing the scaling factor is to reduce the amplitude

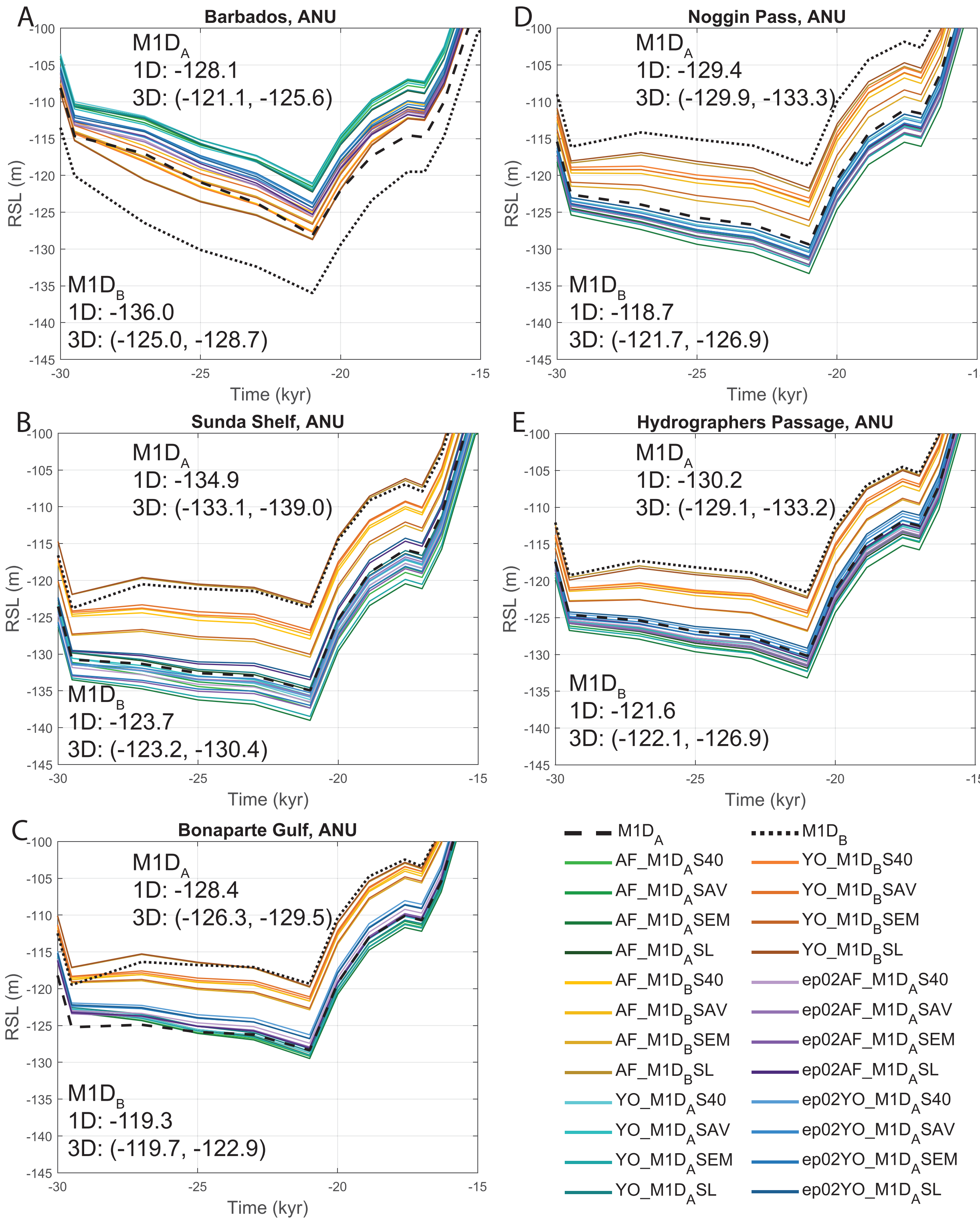

Fig. 5. Relative sea-level curves predicted for all simulations adopting the ANU ice history (Lambeck et al., 2014) from 30 ka to 15 ka at (A) Barbados, (B) Sunda Shelf, (C) Bonaparte Gulf, (D) Noggin Pass, Great Barrier Reef, and (E) Hydrographer's Passage, Great Barrier Reef. Site locations are shown as yellow triangles in Fig. 3. Inset labels specify the full range of predicted RSL at LGM for the 3-D models and the associated 1-D spherically averaged background model. As discussed in the text, we adopt two different background 1-D models, M1D$_A$ and M1D$_B$, for the ANU ice history.

of spatial variability. The results in Table 3 are also suggestive of this correlation, as the simulations with the smaller scaling factor tend to have a smaller signal at all sites considered. This reflects the effect of reducing the scaling factor from temperature to viscosity on the Earth structure, where a smaller scaling factor leads to smaller peak-to-peak variability. The largest impact on the predictions occurs with a change in the choice of seismic model, which alters the geometry of the lateral variations in mantle viscosity, and

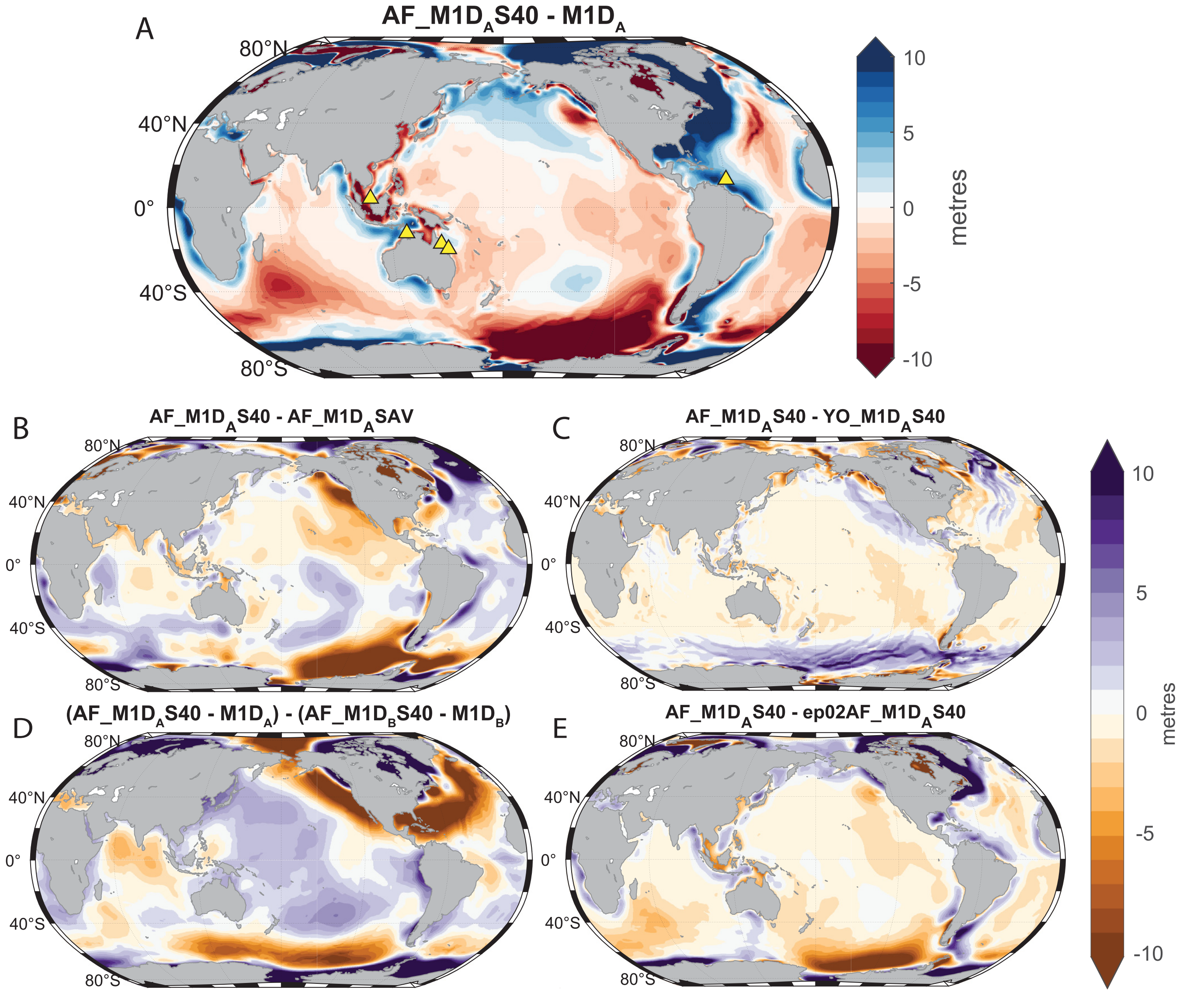

Fig. 6. (A) Difference in RSL (3D minus 1D) at LGM predicted using the ANU ice history (Lambeck et al., 2014) with a 3-D Earth model based on the seismic tomographic model S40RTS of Ritsema et al. (2011), the lithospheric thickness model of Afonso et al. (2019) scaled to give a global mean of 71 km, a temperature-to-viscosity scaling factor of 0.04°C^{-1}, and the M1D$_A$ 1-D viscosity profile. Yellow triangles show the locations of sites in Fig. 5. Results in other frames show the differences between those in A and an identical simulation with the exception that we adopt the (B) seismic model of Auer et al. (2014), (C) lithospheric thickness model of Yousefi et al. (2021), (D) background 1-D model M1D$_B$, and (E) scaling factor from temperature to viscosity of 0.02°C^{-1}.

the spherically averaged (1-D) background model. Regarding the former, as mentioned above, both the amplitude and sign of lateral variations in viscosity differ across different seismic models, which explains the large effect of the choice of seismic model on predicted LGM RSL. Plotting the maximum amplitude of the RSL fields in Fig. 6 (B-E) as a function of latitude shows that all four of these model aspects can contribute significantly at some far-field locations (Fig. S4).

4. Conclusions

The impact of lateral variations in Earth structure on LGM sea-level predictions varies based on location. Of the five far-field sites considered in this study, the largest effect tends to occur at Barbados, with differences in predictions of RSL at LGM between the 3-D and associated 1-D simulations ranging from ~2.5 to 11 m, and a mean of 6.3 m and 6.9 m for the ANU and ICE-6G runs, respectively. The mean impact of lateral variations in viscosity structure at the other 4 sites ranges from <1 m at Bonaparte Gulf to ~3 m at Noggin Pass on the Great Barrier Reef (see Table 3). Notably, the incorporation of lateral structure across all simulations has a consistent effect on predictions at Barbados, shallowing the LGM low stand, and at Noggin Pass, where the predicted low stand is deepened. The former is due to a reduction in ocean loading-induced crustal deformation associated with the high viscosity slab subducting under the Caribbean Plate and/or a change in peripheral bulge dynamics (Austermann et al., 2013). The latter may reflect an amplified continental levering signal due to the thin lithosphere local to the site in both models of global lithospheric thickness we have adopted.

We have considered the impact of varying several aspects that govern the estimated 3-D viscosity structure on the predictions, including the seismic tomography model, spherically averaged (1-D) background viscosity, lithospheric thickness model, and scaling factor that governs the mapping from temperature variations to viscosity. All four aspects are significant and can make a significant difference when considering their effects on sea-level predictions. If we assume that choices in these different model inputs reflect, to some extent, the uncertainty in these aspects for defining 3-D Earth structure, then we conclude that uncertainties in the seismic model and 1-D background model upon which the lateral variations are superimposed make the largest difference in most locations. We also note, as mentioned in the Introduction, that there are other sources of structural uncertainty beyond lateral variations in Earth structure that would affect GIA model output. Our simulations assume a Maxwell viscoelastic Earth, but laboratory experiments and some geodetic data at subduction zones suggest that a Maxwell rheology may not be sufficient (e.g., Ranalli, 2001). Though computationally challenging, recent studies incorporating nonlinear rheology (Kang et al., 2022) or higher order linear rheology (Ivins et al., 2022) in GIA models suggest that these complexities may become important in reconciling observations.

Finally, in the Introduction we discussed the so-called “missing ice” problem, that is, the discrepancy between LGM ice volume estimates based on far-field RSL records versus those based on regional ice sheet reconstructions. For some 3-D models and at some sites, the effect of including lateral variations in Earth structure could help to partially address this problem. However, in all the simulations that we have considered here, there is no consistent, high magnitude signal across all models and at all far-field sites. Thus, we conclude that our analysis does not have significant implications for seeking a solution to this problem. Nevertheless, the impact of lateral variations in Earth structure on predictions of far-field RSL at LGM is both site-dependent and large enough (Fig. 3) such that LGM ice volume estimates should consider multiple sites and be based on 3-D viscoelastic Earth models.

Author statement

Linda Pan: Formal analysis, Investigation, Visualization, Writing – original draft, Writing – review & editing. Glenn A. Milne: Conceptualization, Methodology, Software, Investigation, Writing – review & editing, Supervision. Konstantin Latychev: Methodology, Software, Validation, Writing – review & editing. Samuel L. Goldberg: Methodology, Investigation, Writing – review & editing. Jacqueline Austermann: Conceptualization, Methodology, Writing – review & editing. Mark J. Hoggard: Methodology, Writing – review & editing. Jerry X. Mitrovica: Conceptualization, Supervision, Writing – review & editing.

Declaration of competing interest

The authors declare that they have no known competing financial interests or personal relationships that could have appeared to influence the work reported in this paper.

Acknowledgements

The authors acknowledge PALSEA, a working group of the International Union for Quaternary Sciences (INQUA) and Past Global Changes (PAGES), which in turn received support from the Swiss Academy of Sciences and the Chinese Academy of Sciences. Anthony Purcell, Erik Ivins, and an anonymous reviewer provided constructive comments that helped improve the manuscript. This material is also based upon work supported by the Fonds de Recherche du Québec–Nature et technologies [L.P.], Natural Sciences and Engineering Research Council of Canada [L.P. and G.A.M], Star-Friedman Challenge [L.P. and K.L.], Harvard University Center for the Environment summer research grant [S.L.G.], NSF grant EAR 19-03518 [J.A.], NASA grant NNX17AE17G [M.J.H. and J.X.M.], the Australian Government's *Exploring for the Future* program [M.J.H.], John D. and Catherine T. MacArthur Foundation [J.X.M.], and Harvard University [L.P., K.L., M.J.H., and J.X.M.].

Appendix A. Supplementary data

Supplementary data to this article can be found online at https://doi.org/10.1016/j.quascirev.2022.107644.

References

Abe-Ouchi, A., Saito, F., Kawamura, K., Raymo, M.E., Okuno, J., Takahashi, K., Blatter, H., 2013. Insolation-driven 100,000-year glacial cycles and hysteresis of ice-sheet volume. Nature 500, 190–193.
Afonso, J.C., Salajegheh, F., Szwillus, W., Ebbing, J., Gaina, C., 2019. A global reference model of the lithosphere and upper mantle from joint inversion and analysis of multiple data sets. Geophys. J. Int. 217, 1602–1628.
Audet, P., Burgmann, R., 2011. Dominant role of tectonic inheritance in supercontinent cycles. Nat. Geosci. 4, 184–187.
Auer, L., Boschi, L., Becker, T.W., Nissen-Meyer, T., Giardini, D., 2014. Savani: a variable resolution whole-mantle model of anisotropic shear velocity variations based on multiple data sets. J. Geophys. Res. Solid Earth 119, 3006–3034.
Austermann, J., Mitrovica, J.X., Latychev, K., Milne, G.A., 2013. Barbados-based estimate of ice volume at Last Glacial Maximum affected by subducted plate. Nat. Geosci. 6, 553–557.
Briggs, R.D., Pollard, D., Tarasov, L., 2014. A data-constrained large ensemble analysis of Antarctic evolution since the Eemian. Quat. Sci. Rev. 103, 91–115.
Briggs, R.D., Tarasov, L., 2013. How to evaluate model-derived deglaciation chronologies: a case study using Antarctica. Quat. Sci. Rev. 63, 109–127.
Caron, L., Ivins, E.R., Larour, E., Adhikari, S., Nilsson, J., Blewitt, G., 2018. GIA model statistics for GRACE hydrology, cryosphere, and ocean science. Geophys. Res. Lett. 45, 2203–2212.
Chen, B., Haeger, C., Kaban, M.K., Petrunin, A.G., 2017. Variations of the effective elastic thickness reveal tectonic fragmentation of the Antarctic lithosphere. Tectonophysics 746, 412–424.
Clark, J.A., Farrell, W.E., Peltier, W.R., 1978. Global changes in postglacial sea level: a numerical calculation. Quat. Res. 9, 265–287.
Clark, P.U., Dyke, A.S., Shakun, J.D., Carlson, A.E., Clark, J., Wohlfarth, B., Mitrovica, J.X., Hostetler, S.W., McCabe, A.M., 2009. The last glacial maximum. Science 325, 710–714.
Clark, P.U., Mix, A.C., 2002. Ice sheets and sea level of the last glacial maximum. Quat. Sci. Rev. 21, 1–7.
Clark, P.U., Tarasov, L., 2014. Closing the sea level budget at the last glacial maximum. Proc. Natl. Acad. Sci. U.S.A. 111, 15861–15862.
Cuzzone, J.K., Clark, P.U., Carlson, A.E., Ullman, D.J., Rinterknecht, V.R., Milne, G.A., Lunkka, J.P., Wohlfarth, B., Marcott, S.A., Caffee, M., 2016. Final deglaciation of the Scandinavian Ice Sheet and implications for the Holocene global sea-level budget. Earth Planet Sci. Lett. 448, 34–41.
Denton, G.H., Hughes, T.J., 1981. The Last Great Ice Sheets. Wiley.
Dyke, A.S., Andrews, J.T., Clark, P.U., England, J.H., Miller, G.H., Shaw, J., Veillette, J.J., 2002. The Laurentide and innuitian ice sheets during the last glacial maximum. Quat. Sci. Rev. 21, 9–31.
French, S.W., Romanowicz, B.A., 2014. Whole-mantle radially anisotropic shear velocity structure from spectral-element waveform tomography. Geophys. J. Int. 199, 1303–1327.
Golledge, N.R., Levy, R.H., McKay, R.M., Fogwill, C.J., White, D.A., Graham, A.G.C., Smith, J.A., Hillenbrand, C.D., Licht, K.J., Denton, G.H., Ackert, R.P., Maas, S.M., Hall, B.L., 2013. Glaciology and geological signature of the last glacial maximum Antarctic ice sheet. Quat. Sci. Rev. 78, 225–247.
Gomez, N., Pollard, D., Mitrovica, J.X., 2013. A 3-D coupled ice sheet - sea level model applied to Antarctica through the last 40 ky. Earth Planet Sci. Lett. 384, 88–99.
Gomez, N., Weber, M.E., Clark, P.U., Mitrovica, J.X., Han, H.K., 2020. Antarctic ice dynamics amplified by Northern Hemisphere sea-level forcing. Nature 587, 600–604.
Gowan, E.J., Zhang, X., Khosravi, S., Rovere, A., Stocchi, P., Hughes, A.L.C., Gyllencreutz, R., Mangerud, J., Svendsen, J.-I., Lohmann, G., 2021. A new global ice sheet reconstruction for the past 80 000 years. Nat. Commun. 12, 1199.
Gregory, J.M., Griffies, S.M., Hughes, C.W., Lowe, J.A., Church, J.A., Fukimori, I., Gomez, N., Kopp, R.E., Landerer, F., Le Cozannet, G., Ponte, R.M., Stammer, D., Tamisiea, M.E., van de Wal, R.S.W., 2019. Concepts and terminology for sea level: mean, variability and change, both local and global. Surv. Geophys. 40, 1251–1289.
Hill, A.M., Milne, G.A., Kuchar, J., Ranalli, G., 2019. Sensitivity of glacial isostatic adjustment to a partially molten layer at 410 km depth. Geophys. J. Int. 216, 1538–1548.
Ivins, E.R., Caron, L., Adhikari, S., Larour, E., 2022. Notes on a compressible extended

Burgers model of rheology. Geophys. J. Int. 228, 1975–1991.
Ivins, E.R., James, T.S., Wahr, J., Schrama, E.J.O., Landerer, F.W., Simon, K.M., 2013. Antarctic contribution to sea level rise observed by GRACE with improved GIA correction. J. Geophys. Res. Solid Earth 118, 3126–3141.
Ivins, E.R., van der Wal, W., Wiens, D.A., Lloyd, A.J., Caron, L., 2021. Antarctic Upper Mantle Rheology, vol. 56. Geological Society of London, Memoirs.
Kang, K.X., Zhong, S.J., Geruo, A., Mao, W., 2022. The effects of non-Newtonian rheology in the upper mantle on relative sea level change and geodetic observables induced by glacial isostatic adjustment process. Geophys. J. Int. 228, 1887–1906.
Karato, S.-i., 2008. Deformation of Earth Materials: an Introduction to the Rheology of Solid Earth. Cambridge University Press, Cambridge.
Kendall, R.A., Mitrovica, J.X., Milne, G.A., 2005. On post-glacial sea level - II. Numerical formulation and comparative results on spherically symmetric models. Geophys. J. Int. 161, 679–706.
Lambeck, K., Purcell, A., Zhao, S., 2017. The North American Late Wisconsin ice sheet and mantle viscosity from glacial rebound analyses. Quat. Sci. Rev. 158, 172–210.
Lambeck, K., Rouby, H., Purcell, A., Sun, Y., Sambridge, M., 2014. sea level and global ice volumes from the last glacial maximum to the holocene. Proc. Natl. Acad. Sci. U.S.A. 111, 15296–15303.
Lambeck, K., Smither, C., Johnston, P., 1998. Sea-level change, glacial rebound and mantle viscosity for northern Europe. Geophys. J. Int. 134, 102–144.
Lambeck, K., Yokoyama, Y., Purcell, T., 2002. Into and out of the last glacial maximum: sea-level change during oxygen isotope stages 3 and 2. Quat. Sci. Rev. 21, 343–360.
Latychev, K., Mitrovica, J.X., Tromp, J., Tamisiea, M.E., Komatitsch, D., Christara, C.C., 2005. Glacial isostatic adjustment on 3-D Earth models: a finite-volume formulation. Geophys. J. Int. 161, 421–444.
Lau, H.C.P., Austermann, J., Holtzman, B.K., Havlin, C., Lloyd, A.J., Book, C., Hopper, E., 2021. Frequency dependent mantle viscoelasticity via the complex viscosity: cases from Antarctica. J. Geophys. Res. Solid Earth 126, e2021JB022622.
Lau, H.C.P., Mitrovica, J.X., Austermann, J., Crawford, O., Al-Attar, D., Latychev, K., 2016. Inferences of mantle viscosity based on ice age data sets: radial structure. J. Geophys. Res. Solid Earth 121, 6991–7012.
Lecavalier, B.S., Tarasov, L., 2021. History matching analysis of the Antarctic ice sheet evolution over the last glacial cycle. In: Austermann, J., Simms, A.R. (Eds.), PALSEA-SERCE Virtual Workshop: Improving Understanding of Ice Sheet and Solid Earth Processes Driving Paleo Sea Level Change, p. 13.
Li, T.H., Wu, P., Steffen, H., Wang, H.S., 2018. In search of laterally heterogeneous viscosity models of glacial isostatic adjustment with the ICE-6G_C global ice history model. Geophys. J. Int. 214, 1191–1205.
Li, T.H., Wu, P., Wang, H.S., Steffen, H., Khan, N.S., Engelhart, S.E., Vacchi, M., Shaw, T.A., Peltier, W.R., Horton, B.P., 2020. Uncertainties of glacial isostatic adjustment model predictions in North America associated with 3D structure. Geophys. Res. Lett. 47, e2020GL087944.
Love, R., Milne, G.A., Tarasov, L., Engelhart, S.E., Hijma, M.P., Latychev, K., Horton, B.P., Tornqvist, T.E., 2016. The contribution of glacial isostatic adjustment to projections of sea-level change along the Atlantic and Gulf coasts of North America. Earth's Future 4, 440–464.
Melini, D., Spada, G., 2019. Some remarks on glacial isostatic adjustment modelling uncertainties. Geophys. J. Int. 218, 401–413.
Miller, G.H., Wolfe, A.P., Steig, E.J., Sauer, P.E., Kaplan, M.R., Briner, J.P., 2002. The Goldilocks dilemma: big ice, little ice, or “just-right” ice in the Eastern Canadian Arctic. Quat. Sci. Rev. 21, 33–48.
Milne, G.A., Latychev, K., Schaeffer, A., Crowley, J.W., Lecavalier, B.S., Audette, A., 2018. The influence of lateral Earth structure on glacial isostatic adjustment in Greenland. Geophys. J. Int. 214, 1252–1266.
Mitrovica, J.X., Milne, G.A., 2003. On post-glacial sea level: I. General theory. Geophys. J. Int. 154, 253–267.
Mitrovica, J.X., Wahr, J., Matsuyama, I., Paulson, A., 2005. The rotational stability of an ice-age earth. Geophys. J. Int. 161, 491–506.
Mix, A.C., Bard, E., Schneider, R., 2001. Environmental processes of the ice age: land, oceans, glaciers (EPILOG). Quat. Sci. Rev. 20, 627–657.
Nakada, M., Lambeck, K., 1989. Late Pleistocene and Holocene sea-level change in the Australian region and mantle rheology. Geophys. J. Int. 96, 497–517.
Nakada, M., Okuno, J., Lambeck, K., Purcell, A., 2015. Viscosity structure of Earth's mantle inferred from rotational variations due to GIA process and recent melting events. Geophys. J. Int. 202, 976–992.
Nakada, M., Okuno, J., Yokoyama, Y., 2016. Total meltwater volume since the Last Glacial Maximum and viscosity structure of Earth's mantle inferred from relative sea level changes at Barbados and Bonaparte Gulf and GIA-induced J2. Geophys. J. Int. 204, 1237–1253.
Paulson, A., Zhong, S.J., Wahr, J., 2007. Inference of mantle viscosity from GRACE and relative sea level data. Geophys. J. Int. 171, 497–508.
Peltier, W.R., 2004. Global glacial isostasy and the surface of the ice-age earth: the ice-5G (VM2) model and GRACE. Annu. Rev. Earth Planet Sci. 32, 111–149.
Peltier, W.R., Argus, D.F., Drummond, R., 2015. Space geodesy constrains ice age terminal deglaciation: the global ICE-6G_C (VM5a) model. J. Geophys. Res. Solid Earth 120, 450–487.
Peltier, W.R., Fairbanks, R.G., 2006. Global glacial ice volume and Last Glacial Maximum duration from an extended Barbados sea level record. Quat. Sci. Rev. 25, 3322–3337.
Ranalli, G., 2001. Mantle rheology: radial and lateral viscosity variations inferred from microphysical creep laws. J. Geodyn. 32, 425–444.
Raymo, M.E., Kozdon, R., Evans, D., Lisiecki, L., Ford, H.L., 2018. The accuracy of mid-Pliocene δ18O-based ice volume and sea level reconstructions. Earth Sci. Rev. 177, 291–302.
Ritsema, J., Deuss, A., van Heijst, H.J., Woodhouse, J.H., 2011. S40RTS: a degree-40 shear-velocity model for the mantle from new Rayleigh wave dispersion, teleseismic traveltime and normal-mode splitting function measurements. Geophys. J. Int. 184, 1223–1236.
Roy, K., Peltier, W.R., 2017. Space-geodetic and water level gauge constraints on continental uplift and tilting over North America: regional convergence of the ICE-6G_C (VM5a/VM6) models. Geophys. J. Int. 210, 1115–1142.
Schaeffer, A.J., Lebedev, S., 2013. Global shear speed structure of the upper mantle and transition zone. Geophys. J. Int. 194, 417–449.
Simms, A.R., Lisiecki, L., Gebbie, G., Whitehouse, P.L., Clark, J.F., 2019. Balancing the last glacial maximum (LGM) sea-level budget. Quat. Sci. Rev. 205, 143–153.
Simon, K.M., Riva, R.E.M., 2020. Uncertainty estimation in regional models of long-term GIA uplift and sea level change: an overview. J. Geophys. Res. Solid Earth 125, e2019JB018983.
Steffen, R., Audet, P., Lund, B., 2018. Weakened lithosphere beneath Greenland inferred from effective elastic thickness: a hot spot effect? Geophys. Res. Lett. 45, 4733–4742.
Tarasov, L., Dyke, A.S., Neal, R.M., Peltier, W.R., 2012. A data-calibrated distribution of deglacial chronologies for the North American ice complex from glaciological modeling. Earth Planet Sci. Lett. 315–316, 30–40.
van der Wal, W., Barnhoorn, A., Stocchi, P., Gradmann, S., Wu, P., Drury, M., Vermeersen, B., 2013. Glacial isostatic adjustment model with composite 3-D Earth rheology for Fennoscandia. Geophys. J. Int. 194, 61–77.
Waelbroeck, C., Labeyrie, L., Michel, E., Duplessy, J.C., McManus, J.F., Lambeck, K., Balbon, E., Labracherie, M., 2002. Sea-level and deep water temperature changes derived from benthic foraminifera isotopic records. Quat. Sci. Rev. 21, 295–305.
Whitehouse, P.L., Bentley, M.J., Le Brocq, A.M., 2012. A deglacial model for Antarctica: geological constraints and glaciological modelling as a basis for a new model of Antarctic glacial isostatic adjustment. Quat. Sci. Rev. 32, 1–24.
Wu, P., Wang, H.S., 2008. Postglacial isostatic adjustment in a self-gravitating spherical earth with power-law rheology. J. Geodyn. 46, 118–130.
Yokoyama, Y., Esat, T.M., Thompson, W.G., Thomas, A.L., Webster, J.M., Miyairi, Y., Sawada, C., Aze, T., Matsuzaki, H., Okuno, J., Fallon, S., Braga, J.-C., Humblet, M., Iryu, Y., Potts, D.C., Fujita, K., Suzuki, A., Kan, H., 2018. Rapid glaciation and a two-step sea level plunge into the Last Glacial Maximum. Nature 559, 603–607.
Yokoyama, Y., Lambeck, K., De Deckker, P., Johnston, P., Fifield, L.K., 2000. Timing of the last glacial maximum from observed sea-level minima. Nature 406, 713–716.
Yousefi, M., Milne, G.A., Latychev, K., 2021. Glacial isostatic adjustment of the Pacific Coast of North America: the influence of lateral Earth structure. Geophys. J. Int. 226, 91–113.